Draft version November 10, 2025
Typeset using LaTeX **twocolumn** style in AASTeX7.0.1

arXiv:2507.20684v2 [astro-ph.GA] 7 Nov 2025

A deep dive down the broad-line region: permitted O I, Ca II and Fe II emission in an AGN Little Red Dot at $z = 5.3$

Roberta Tripodi [1,2,3] Maruša Bradač [2] Francesco D'Eugenio [4,5] Nicholas Martis [2] Gregor Rihtaršič [2] Chris Willott [6] Laura Pentericci [1] Bianca Moreschini, [7,8] Maxim Markevitch [9] Yoshihisa Asada [10] Antonello Calabrò [1] Guillaume Desprez [11] Giordano Felicioni, [2] Gaia Gaspar [12] Anthony H. Gonzalez [13] Anishya Harshan [2] Xihan Ji [4,5] Jon Judež [2] Brian C. Lemaux [14,15] Alessandro Marconi [7,8] Vladan Markov [2] Rosa M. Merida [12] Lorenzo Napolitano [1] Gaël Noirot, [16] Massimiliano Parente [17] Annika H. G. Peter [18] Luke Robbins [19] Andrew Robertson [20] Ghassan T. E. Sarrouh [21] and Marcin Sawicki [12]

[1] *INAF - Osservatorio Astronomico di Roma, Via Frascati 33, I-00078 Monte Porzio Catone, Italy*
[2] *University of Ljubljana FMF, Jadranska 19, 1000 Ljubljana, Slovenia*
[3] *IFPU - Institute for Fundamental Physics of the Universe, via Beirut 2, I-34151 Trieste, Italy*
[4] *Kavli Institute for Cosmology, University of Cambridge, Madingley Road, Cambridge CB3 0HA, UK*
[5] *Cavendish Laboratory - Astrophysics Group, University of Cambridge, 19 JJ Thomson Avenue, Cambridge, CB3 0HE, UK*
[6] *NRC Herzberg, 5071 West Saanich Rd, Victoria, BC V9E 2E7, Canada*
[7] *Dipartimento di Fisica e Astronomia, Università di Firenze, Via G. Sansone 1, 50019 Sesto F.no (Firenze), Italy*
[8] *INAF-Osservatorio Astrofisico di Arcetri, Largo E. Fermi 5, 50125 Firenze, Italy*
[9] *NASA / Goddard Space Flight Center, Greenbelt, MD 20771, USA*
[10] *Waseda Research Institute for Science and Engineering, Faculty of Science and Engineering, Waseda University, 3-4-1 Okubo, Shinjuku, Tokyo 169-8555, Japan*
[11] *Kapteyn Astronomical Institute, University of Groningen, P.O. Box 800, 9700AV Groningen, The Netherlands*
[12] *Department of Astronomy and Physics and Institute for Computational Astrophysics, Saint Mary's University, 923 Robie Street, Halifax, B3H 3C3, Nova Scotia*
[13] *Department of Astronomy, University of Florida, Bryant Space Science Center, Gainesville, FL 32611, USA*
[14] *Gemini Observatory, NSF NOIRLab, 670 N. A'ohoku Place, Hilo, Hawai'i, 96720, USA*
[15] *Department of Physics and Astronomy, University of California, Davis, One Shields Ave., Davis, CA 95616, USA*
[16] *Space Telescope Science Institute, 3700 San Martin Drive, Baltimore, Maryland 21218, USA*
[17] *INAF - Observatory of Trieste, Via G.B. Tiepolo 11, 34131, Trieste, Italy*
[18] *Department of Physics, Department of Astronomy, and CCAPP, The Ohio State University*
[19] *Department of Physics and Astronomy, Tufts University, 574 Boston Avenue, Suite 304, Medford, MA 02155, USA*
[20] *Carnegie Observatories, 813 Santa Barbara Street, Pasadena, CA 91101, USA*
[21] *Department of Physics and Astronomy, York University, 4700 Keele St. Toronto, Ontario, M3J 1P3, Canada*

ABSTRACT

We present a spectroscopic analysis of a broad-line active galactic nucleus (AGN) selected as little red dot at $z = 5.3$ behind the Bullet cluster (Bz5.3), based on *JWST*/NIRCam and NIRSpec data. The detection of strong Fe II, O I, and Ca II triplet emission lines, along with the evidence of broad Balmer lines, provides strong evidence of a broad-line region (BLR) and an accreting supermassive black hole. Notably, we report the first detection of the λ1304 bump (i.e., blend of O Iλ1304 and Si II) at high redshift, a feature commonly seen in local AGNs but not yet reported in the early Universe. The O Iλ1304/λ8446 photon ratio provides an independent measurement of dust attenuation in galaxies. In Bz5.3, this ratio is highly suppressed (0.1–0.3), implying significant internal dust extinction, with estimated dust attenuation $A_V \sim 0.4$–1.0. We identify Lyβ fluorescence as the dominant excitation mechanism of the low-ionization lines, with additional contributions from collisional excitation. High O Iλ8446 equivalent width and weak O Iλ7774 support this interpretation. The detection of iron emission, whether from broad permitted or narrow forbidden lines, supports the presence of a stratified BLR, as also recently proposed in local LRDs. Photoionization modeling of O Iλ8446 and Ca II further suggests the coexistence of multiple gas phases with distinct densities and ionization states, highlighting the complexity of the BLR. Bz5.3 thus offers a rare window into early AGN activity and BLR physics at early times.

Email: roberta.tripodi@inaf.it

Keywords: Astrophysical black holes (98), AGN host galaxies (2017), Galaxy spectroscopy (2171)

1. INTRODUCTION

The Broad Line Region (BLR) — a compact, high-density ($n_{\rm h} \sim 10^9$–10^{10} cm^{-3}) and high-velocity (FWHM $\sim$ 1000–10000 km s^{-1}) region within $\lesssim$ 1 pc of a supermassive black hole (SMBH) — produces the broad emission lines observed in active galactic nuclei (AGNs). These lines, including Balmer lines, Mg II, C IV, Fe II, O I, and the Ca II triplet, provide key insights into the structure, kinematics, and chemical composition of the gas surrounding SMBHs (see H. Netzer 2013). Among them, low-ionization lines (LILs) like Fe II, O I, and Ca IIλ8498,8542,8662 are especially valuable for probing the outer BLR.

Understanding the excitation and distribution of UV–optical iron emission is crucial, as Fe II is a major coolant of the BLR and reflects the gas energy budget (B. J. Wills et al. 1985; Y. Matsuoka et al. 2007). Its emission also traces chemical enrichment across cosmic time (F. Hamann & G. Ferland 1999, 1993; Y. Yoshii et al. 1998). The main excitation mechanisms are Lyα fluorescence and collisional excitation (S. A. Grandi 1980; A. Rodríguez-Ardila et al. 2002), with near-IR Fe II lines especially linked to the former. Thanks to studies using reverberation mapping, Fe II is found to arise in the outer BLR, where its spectral profile and equivalent width encode the physical conditions (J. Kovačević et al. 2010; J. A. Baldwin et al. 2004). Interestingly, UV Fe II features have recently been reported in two AGN "Little Red Dots" (LRDs), A2744-45924 at $z = 4.47$ (I. Labbe et al. 2024) and CAPERS-LRD-z9 at $z = 9.288$ (A. J. Taylor et al. 2025), directly linking them to BLR origin. It is still unknown whether these UV features are widespread but weak, or if they emerge in certain LRDs due to specific BH properties or geometric effects such as inclination or the distribution of dust. In contrast, optical Fe II lines are typically weak in JWST-selected broad-line AGN, possibly due to the reduced metallicity of their broad line region (B. Trefoloni et al. 2024). Despite the large number of studies of Fe II in AGNs (e.g., P. Marziani et al. 2013; H. Netzer & B. J. Wills 1983; B. J. Wills et al. 1985; T. A. A. Sigut & A. K. Pradhan 1998, 2003; E. M. Verner et al. 1999; E. Verner et al. 2003, 2004; J. A. Baldwin et al. 2004; Y. Tsuzuki et al. 2006; R. J. Rudy et al. 2000; X.-B. Dong et al. 2009; J. Kovačević-Dojčinović et al. 2025; I. Labbe et al. 2024; B. Trefoloni et al. 2024; G. J. Ferland et al. 2020), interpreting the blended Fe II pseudo-continuum remains challenging given the complex energy levels of Fe II and the mixed excitation mechanisms. In detail, the Fe II emission is usually modeled by adopting templates generated by different photoionization models. However, models exhibit a high level of degeneracy when compared to the observed data, especially when the sensitivity and the spectral resolution of the data are low.

Complementary diagnostics come from simpler atoms thought to trace similar BLR regions and excitation conditions. Neutral oxygen (O I) and singly-ionized calcium (Ca II) often correlate with Fe II in strength and width (A. Rodríguez-Ardila et al. 2002; M. Joly 1987; Y. Matsuoka et al. 2007, 2008; P. Marziani et al. 2013; G. J. Ferland & S. E. Persson 1989; S. E. Persson 1988), reflecting their comparable ionization potentials (16.2, 13.6, and 11.9 eV for Fe II, O I, and Ca II, respectively). The O Iλ8446 line lacks a narrow component and is associated with Lyβ fluorescence (S. A. Grandi 1980; R. J. Rudy et al. 1989). Emission at O Iλ1304, O Iλ8446, and O Iλ11287 is expected in a 1:1:1 photon ratio, with deviations indicating alternative mechanisms like recombination or collisional excitation (A. Laor et al. 1997; A. Rodríguez-Ardila et al. 2002; Y. Matsuoka et al. 2005, 2007, 2008). The O Iλ1304 line is usually found blended with the Si II line, which constitutes the so-called λ1304 bump. Additional O I lines such as O Iλ7774 and O Iλ7990 help refine the dominant processes.

Ca II emission arises primarily from the near-IR triplet (Ca IIλ8498,8542,8662), emitted from neutral, optically thick gas shielded from hard radiation (G. J. Ferland & S. E. Persson 1989; M. Joly 1989). Comparisons between Ca IIλ8498,8542,8662, O I, and Fe II emission, both in flux and kinematics, constrain the gas density, ionization, and geometry of the BLR (Y. Matsuoka et al. 2007, 2008).

Y. Matsuoka et al. (2008) found that these diagnostics in low-redshift quasars ($z < 1$) show little redshift or luminosity dependence, suggesting similar gas densities and ionizing fields, possibly mixed with dust.

Until now, such studies have been largely limited to $z < 1$ due to sensitivity and resolution limits. Only a few exceptions exist at higher redshifts: 4 quasars at $z \sim 2.1$ with weak O Iλ1304 detection (B. R. Espey et al. 1989), a $z \sim 2.26$ "Rosetta Stone" quasar with Ca II emission (I. Juodžbalis et al. 2024), and the $z \sim 4.5$ LRD A2744-45924 with O I, Ca IIλ8498,8542,8662. After the discovery of the λ1304 bump in Bz5.3, O Iλ1304 has been detected in CANUCS-LRD-z8.6, an LRD at z=8.6 (T. Morishita et al. 2025).

In this Letter, we present the discovery of Bullet-LRD-z5.3 (hereafter Bz5.3), an AGN host at $z_{\rm spec} = 5.2907 \pm 0.0002$, magnified by a factor $\mu = 3.7^{+0.2}_{-0.1}$. Using *JWST*/NIRSpec prism spectroscopy, we report the first detection of the λ1304 bump at $z > 5$, along with strong O Iλ8446, Ca IIλ8498,8542,8662, and rest-UV/optical Fe II emission. These observations offer a rare opportunity to probe BLR structure and excitation at early cosmic times. Data are pre-

sented in Sect. 2, results in Sect. 3, discussion in Sect. 4, and conclusions in Sect. 5.

Throughout the paper we adopt the ΛCDM cosmology from Planck Collaboration et al. (2020): H_0 = 67.4 km s^{-1} Mpc^{-1}, Ω_m = 0.315, and Ω_Λ = 0.685. Thus, the angular scale is 6.238 kpc/arcsec at z = 5.2907.

2. DATA

The Bullet cluster was observed with NIRCam (M. J. Rieke et al. 2023) in *JWST* Cycle 3 in January 2025 (GO program 4598, PI Bradač). We obtained imaging in eight filters, F090W, F115W, F150W, F200W, F277W, F356W, F410M and F444W with exposure times of ∼ 6.4 ks each. In addition we use the archival HST/ACS observations in F606W, F775W and F850LP filters (programs 10200 and 10863, PI Jones & Gonzalez) and F814W filter (program 11099, PI Bradač). The images were processed with a modified version of the stage 1 and stage 2 JWST pipeline, the Canadian NIRISS Unbiased Cluster Survey (CANUCS) data reduction pipeline (full details in G. T. E. Sarrouh et al. 2025), before being drizzled onto a 40 milliarcsec pixel grid using the `grizli` code (G. Brammer 2019). Bright cluster and foreground galaxies as well as intracluster light are removed from the images following the procedure outlined in N. S. Martis et al. (2024). Photometry is performed on the subtracted, psf-matched images convolved to the F444W filter resolution.

Bz5.3 was photometrically selected as an LRD using the NIRCam data, following standard color and compactness criteria (V. Kokorev et al. 2024). Specifically, F115W-F150W< 0.8, F200W-F277W> 0.7, F200W-F356W> 1.0, and the compactness in F444W is < 1.7. Bz5.3 was followed up with NIRSpec/prism ($R \sim 30 - 400$) with the Micro-Shutter Assembly (MSA) as part of the same GO program 4598. NIRSpec/prism data have also been reduced and the redshift of the source has been estimated following the procedure described in G. T. E. Sarrouh et al. (2025). From the 2D spectral reduction, a 1D spectrum is extracted using an optimal extraction based on the source spatial profile. We correct for slit losses by scaling the 1D spectrum to the observed photometry. Specifically, we perform photometry in the region covered by the MSA slit, then fit a Chebyeshev polynomial to the ratio of the observed photometry and synthetic photometry obtained from convolving the spectrum within each filter. The 1D spectrum is then multiplied by the derived polynomial.

To estimate magnification due to lensing, a strong lensing model was derived using the parametric lens modeling tool `Lenstool` (J. P. Kneib et al. 1996; E. Jullo et al. 2007; E. Jullo & J. P. Kneib 2009) and is constrained with a catalogue of 141 multiple images from 28 background galaxies with spectroscopic redshifts. The catalogue of multiple images was derived using JWST data. It includes multiple image candidates included in S. Cha et al. (2025) lens model, harnessing NIRCam imaging, and adds additional systems and NIRSpec spectroscopic redshifts for 22 galaxies. The model includes large-scale dark matter halos, cluster member subhalos, cluster gas, included as a mass map from Chandra X-ray observations, and group-scale substructure halos surrounding the cluster. The derived magnification of Bz5.3 is $\mu = 3.7^{+0.2}_{-0.1}$. For the discussion of the lens model and the catalogues of strong lensing constraints see Rihtaršič et al, in prep. Unless otherwise specified, quantities are corrected for magnification. Magnification uncertainties are added in quadrature to the statistical uncertainties in fluxes, and introduce -on average- a systematic error of 0.03 dex in the flux and luminosities measurements. Magnification uncertainties are typically subdominant with respect to the statistical uncertainties on the fluxes. Reported errors on black hole mass estimates include propagation of magnification uncertainties.

An inspection of the available Chandra 500 ks data targeting the Bullet Cluster (D. Clowe et al. 2006) reveals no significant X-ray point source at the position of Bz5.3, consistent with the lack of X-ray detections reported in other LRD samples (T. T. Ananna et al. 2024; M. Yue et al. 2024; A. Sacchi & A. Bogdan 2025). A 3σ upper limit on the point source unabsorbed X-ray flux in the 0.5–2 kev observer band is 1.2×10^{-7} phot cm^{-2} s^{-1}, with the uncertainty dominated by the relatively bright diffuse emission of the galaxy cluster plasma at this position. At z = 5.29 and assuming μ =3.7, this corresponds to the rest-frame 3–12 keV intrinsic luminosity of $L_X < 1.6 \times 10^{43}$ erg s^{-1}.

3. ANALYSIS AND RESULTS

Figure 1 show the 2D and 1D spectra of Bz5.3, along with all the available NIRCam photometry of the source. Bz5.3 is a point source in F444W and F410M, while shows extended emission in all the other filters (see App. A for more details). Based on the flux centroids, we find no significant spatial variation ($\lesssim 0.04''$) between the emitting region in the bluest UV (F814w) and in near UV (F150W).

The blue UV slope ($\beta_{\rm UV,spec} = -1.6 \pm 0.1$), red optical slope ($\beta_{\rm opt,spec} = 0.66 \pm 0.09$), and compactness in F444W together classify Bz5.3 as an LRD, in compliance with the standard criteria reported in V. Kokorev et al. (2024) and D. D. Kocevski et al. (2025).

Several clear AGN signatures and a prominent Balmer break are evident upon visual inspection of the spectra. Notably, we detect Lyα, O Iλ1304, N IV], C IV, C III], Mg II and Fe II, [O II], [Ne III]$\lambda\lambda$3869,3967, Hδ, Fe IIλ4278, Hγ, narrow Hβ, He Iλ4471, [O III]λ5007, Fe IIλ5165 λ5274λ5335, He Iλ5877, [N II]λ6584, narrow Hα, [S II], He Iλ7067, O Iλ8446, Ca IIλ8498,8542,8662, emission lines, as well as broad Hα emission with a full width at half maximum (FWHM) of 4600 ± 50 km s^{-1}, and broad Hβ emission with

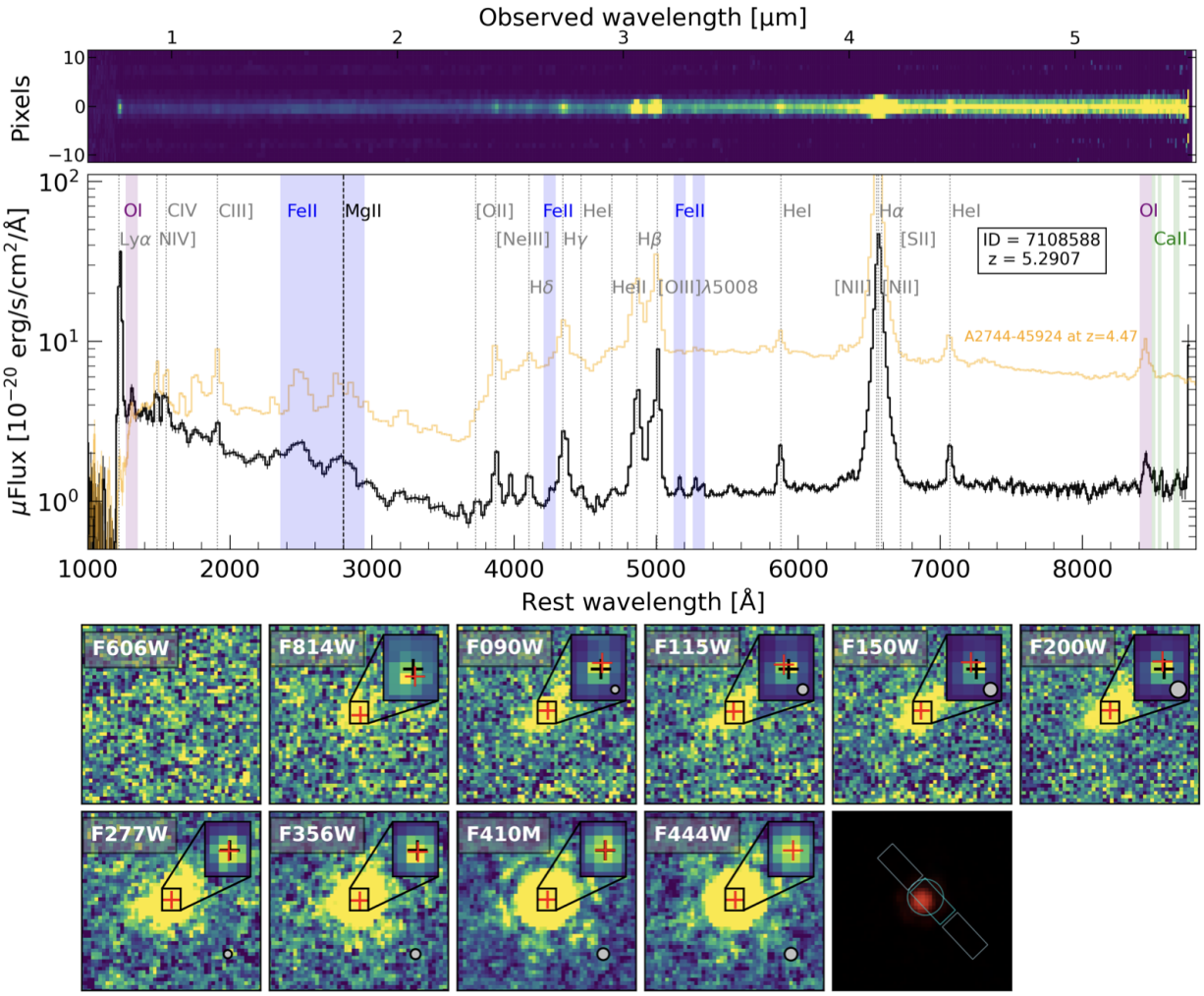

Figure 1. HST/ACS and NIRCam photometry, and NIRSpec spectra of Bz5.3. Top panels: 2D and 1D NIRSpec spectra. Fluxes are not corrected for magnification. Lines of interest for this work are highlighted by colored vertical bars. Other detected emission lines are marked with dashed gray vertical lines. The y-axis scale of the 1D spectrum is logarithmic. For comparison the spectrum of A2744-45924 at $z = 4.47$ is shown in light orange. Bottom panels: NIRCam cut-out photometry in different filters, specified at the top left corner of each panel, and RGB image made combining the F444W, F356W, and F277W for red, F150W and F200W for green, and F090W and F115W filters for blue. Cutouts images are 2"×2" in size. In each panel, there is an inset zooming-in on the center region to show the flux centroid of the filter (red cross), compared to the flux centroid in F444W (black cross). The PSF size of each NIRCam filter is shown as a gray circle in the bottom right corner of each panel (or zoom-in inset).

FWHM = 5100 ± 500 km s^{-1}. Using the virial relation from A. E. Reines & M. Volonteri (2015)[4], this broad Hα line implies a black hole (BH) mass of $\log(M_{\rm BH}/{\rm M}_\odot) = 8.4 \pm 0.3$. This implies an Eddington ratio of $\lambda_{\rm Edd} = 0.008^{+0.016}_{-0.005}$, having derived the bolometric luminosity $\log(L_{\rm bol}/{\rm erg\ s^{-1}}) = 44.4 \pm 0.5$ from the continuum luminosity at 3000 Å, adopting the bolometric correction from G. T. Richards et al. (2009). Analogously, using the virial relations from J. E. Greene & L. C. Ho (2005) and M. Vestergaard & B. M. Peterson (2006)[5] for the broad Hβ line and having $L_{\rm H\beta,broad} = 7.8^{+2.4}_{-1.9} \times 10^{41}$ erg/s from our best-fit model, we derive a BH mass of $\log(M_{\rm BH}/{\rm M}_\odot) = 7.9 \pm 0.3$, which is fully consistent with the one from Hα.

In this work, however, we focus on the discussion of the BLR properties as derived from the O I, Ca II, and Fe II emission lines. Therefore, in this section, we describe the fitting methodology and present the results for these lines only. A complete analysis and discussion of the other source's prop-

[4] A. E. Reines & M. Volonteri (2015) assumed a mean scale factor of $f = 4.3$ (C. J. Grier et al. 2013).

[5] J. E. Greene & L. C. Ho (2005) assumed a scale factor of $f = 0.75$ (S. Kaspi et al. 2000), while M. Vestergaard & B. M. Peterson (2006) assumed $f = 5.5 \pm 1.9$ (C. A. Onken et al. 2004).

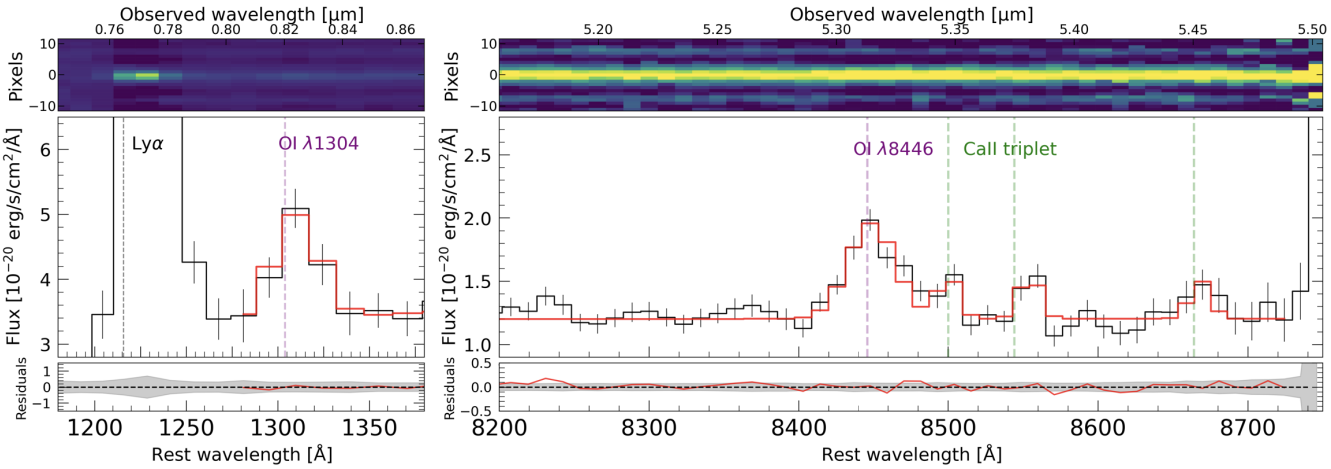

Figure 2. Zoom-in of the 2D and 1D spectra of Bz5.3. The observed spectrum is shown in black, and the best-fitting model is shown in red. Residuals are shown at the bottom of each panel, where the shaded gray area represents the 1σ noise level. Left panel: zoom on the λ1304 bump. The vertical pink line is at the laboratory rest wavelength of the O I λ1304 emission line. The vertical dashed black line marks the Lyα line. Right panel: zoom-in on the O I λ8446 emission line and on the Ca II λ8498,8542,8662 triplet. Vertical lines are set at laboratory rest wavelength for these emission lines. The scale of the y-axis is linear.

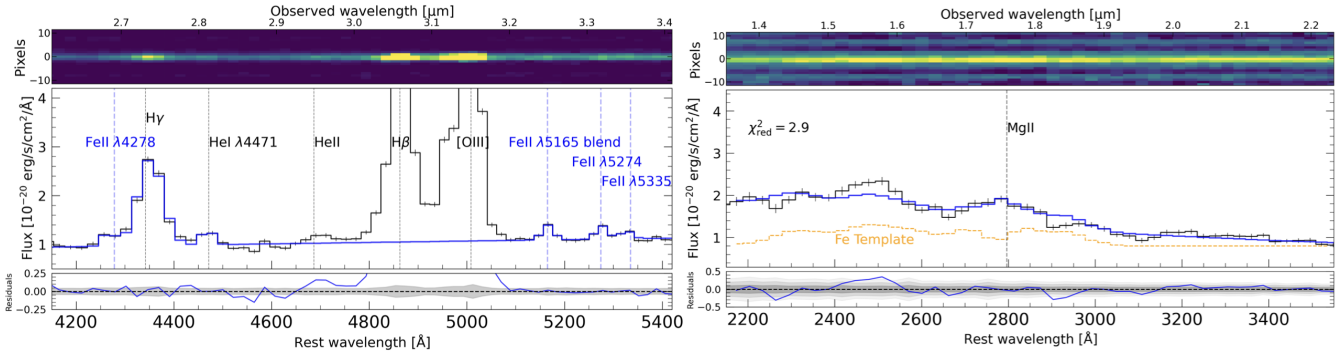

Figure 3. Zoom-in of the 2D and 1D spectra of Bz5.3. The observed spectrum is shown in black, while the best-fitting model is shown in blue. Residuals are shown at the bottom of each panel, where the shaded dark gray area represents the 1σ noise level. Top panel: zoom on the Fe II emission in the optical. The vertical lines are at the laboratory rest wavelength of the reported emission line. Bottom panel: zoom on the Fe II complex in the UV and Mg II emission line. 2 and 3σ noise levels are reported in the residual as shaded lighter gray area.

erties is deferred to a following and more extensive work (Tripodi et al., in prep.).

3.1. *Continuum and line fitting*

The underlying continuum of the λ1304 bump and of O I λ8446 + Ca II λ8498,8542,8662 is modeled separately using a linear relation[6] and power-law, respectively, both with free slope and normalization. Each emission line is modeled as a single Gaussian.

The FWHM is fixed to be the same for each line in the Ca II λ8498,8542,8662 triplet. The relative intrinsic ratio of the triplet is found to be 1:9:5 in an optically thin regime, and flattens to 1:1:1 for optically thick media, as derived from analysis of stars (M. G. Guarcello et al. 2014). R. J. Rudy et al. (2000) found that, in the AGN I Zw 1, this ratio is 1:1.15:0.83 probably due to different gas conditions w.r.t a simple optically thick homogeneous medium, and this assumption has been adopted also in the analysis of quasars by Y. Matsuoka et al. (2008). Given the lack of precise prescriptions in this regard, we choose to leave the flux relative intensities free and see whether our results align, or not, with the above mentioned values.

As mentioned in Sect. 1, modeling the Fe II pseudo-continuum is particularly challenging, and empirical templates from low-redshift well-studied sources are often used to fit the observed data (e.g. I. Labbe et al. 2024). In particular, we adopted the template either from M. Vestergaard & B. J. Wilkes (2001) or from Y. Tsuzuki et al. (2006) to model the Fe II signatures in the UV, which are also blended with

[6] The linear relation provided a better model for the underlying continuum of the λ1304 bump than a power-law given that the available wavelength range of continuum emission is small, since the bump lies close to the Lyα and N V emission.

the Mg II emission. Alternatively, we also produced Fe II templates from tailored photo-ionization models (see Appendix C for details). The Mg II line is fitted with a single Gaussian, and the underlying continuum with a power-law relation as described above. The template has been convolved with the resolution of the instrument.

The Fe II emission lines detected in the optical, Fe IIλ4278, Fe IIλ5165, Fe IIλ5274 and Fe IIλ5335, are modeled as a single Gaussian each, and the underlying continuum as a power law. We do not adopt empirical templates since some of the observed intensities of optical Fe II lines are not as theoretically expected (see Sect .4 and J. Kovačević-Dojčinović et al. 2025). The FWHM of all these transitions is fixed to be the same, since they are thought to arise from the same region. Fe IIλ4278 is blended with Hγ + [O III]λ4364 and He I λ4471, therefore we also model Hγ +[O III]λ4364 and He I λ4471 as two independent Gaussians. Other emission lines at 4200Å < $\lambda_{\rm rest}$ < 5400Å have been masked. The results of the fit are shown in Figure 2 for the O I and Ca II complexes, and in Figure 3 for Fe II and Mg II.

Details on the specific fitting procedure used and the derivation of the measured quantities can be found in Appendix B. Flux, FWHM and EW of all the fitted lines are reported in Table 1. FWHMs are corrected for instrumental broadening (see Appendix B for details).

3.2. *Constitution of the λ1304 Bump*

The λ1304 bump typically seen in AGN spectra is the result from a blending of an O I triplet at λ1302.17, λ1304.86, and λ1306.03 (named so far as O Iλ1304), and a Si II doublet at λ1304.37 and λ1309.27 (hereafter just Si II). The blending is usually very strong in most quasars, preventing a reliable estimate of the relative contributions of O I and Si II to the blend. However, A. Laor et al. (1997) were able to estimate the O I and Si II fractions in the blend for I Zw 1, given that the Si II was clearly detected. They found that 50% (56%) of the bump flux is due to O I in the optically thin (thick) Si II doublet case. Moreover, A. Rodríguez-Ardila et al. (2002) estimated that in three narrow-line Seyfert 1 galaxies the average proportion of the O I flux is 75%, while Y. Matsuoka et al. (2007) reported a larger range of O I fractions in 5 quasars at $0.15 < z < 1.1$, ranging from 20% to 98%. Y. Matsuoka et al. (2007) also presented some theoretical considerations regarding the possible strengthening of the Si II line: in particular, Si II flux can be enhanced in the large optically emitting cloud (LOC) scenario or in a gas with unusually large micro-turbulent velocities (as also suggested by M. Bottorff et al. 2000). The latter scenario, however, implies a significant suppression in the Lyβ fluorescence rate, which is not our case as discussed in Sect. 4.4.

The spectral resolution of our data prevents us from resolving the bump; therefore, we fit the bump with a single Gaussian. For the following calculations, we assume a O Iλ1304 fraction of 50% to correct for the Si II contamination, which corresponds -on average- to the results found in literature.

Table 1. Results from the emission line fitting procedure

Line	μFlux [10^{-18} erg s^{-1} cm^{-2}]	FWHM [km s^{-1}]	EW [Å]
O Iλ1304 †	$3.2^{+1.4}_{-1.0}$	–	15^{+8}_{-6}
O Iλ7774	< 0.4	–	–
O Iλ7790	< 0.5	–	–
O Iλ8446	1.86 ± 0.15	940^{+50}_{-100}	25 ± 2
Ca IIλ8498	$0.39^{+0.13}_{-0.11}$	–	5.7 ± 1.5
Ca IIλ8542	0.40 ± 0.11	–	5.4 ± 1.5
Ca IIλ8662	$0.34^{+0.16}_{-0.14}$	–	4.6 ± 2
Fe IIλ4278	0.609 ± 0.108	–	9 ± 2
Fe IIλ5165	$0.588^{+0.094}_{-0.091}$	–	9 ± 1
Fe IIλ5274	$0.528^{+0.083}_{-0.079}$	–	7 ± 1
Fe IIλ5335	0.313 ± 0.077	–	4 ± 1
Mg II	1.98 ± 0.34	–	24 ± 4

Notes. Fluxes reported here are not corrected for magnification. † Results reported here do not consider the possible contamination from Si II.

3.3. *Emission line measurements*

Here we present the results obtained by performing the fit of the lines of interest in Bz5.3 using the method described in Sect. 3.1. These are also summarized in Table 1.

O Iλ1304,7774,7790,8446. We clearly detect both the λ1304 bump at S/N = 5, and λ8446 at S/N= 9.6, while λ7774 and λ7790 remain undetected. Given that the prism spectral resolution (R) increases by a factor of 10 between $\lambda_{\rm rest}$ = 1304 Å and $\lambda_{\rm rest}$ = 8446 Å, the λ1304 bump remains unresolved, while for λ8446 we measure a broadening of FWHM = 940^{+50}_{-100} km s^{-1}. The measured observed fluxes are reported in Table 1. Given these estimates, we derive the following flux ratios for λ7774, λ7790 over λ8446: $r_{7774/8446} < 0.23$, $r_{7790/8446} < 0.28$. To estimate the upper limit on flux ratio between λ1304 and λ8446 we assuming a fraction of O Iλ1304 of 100%, implying $r_{1304/8446} \leq 1.7^{+0.8}_{-0.6}$. If assuming the contamination of Si II λ1309 on the O Iλ1304 to be of order 50% (see Sect. 3.2 for discussion), the flux ratio becomes $r_{1304/8446,\rm corr} = 0.9 \pm 0.3$. These correspond to photon flux ratios of $\rm ROI_{UV} < 0.27^{+0.12}_{-0.09}$, and $\rm ROI_{UV,corr} \leq 0.13^{+0.06}_{-0.04}$, respectively[7].

[7] The photon flux ratio (region of interest or ROI) between two emission lines, at λ_i and λ_j, is defined as $\rm ROI_{ij} = n(\lambda_i)/n(\lambda_j)$, where $n(\lambda_i) = F^i_\lambda/E_i$ [*photons* s^{-1} cm^{-2}] is the photon flux of the line i with flux F^i_λ [erg s^{-1} cm^{-2}] and with energy of the emitting photons $E_i = hc/\lambda_i$ [erg].

Ca II λ8498,8542,8662 triplet. Each line in the calcium triplet is detected with S/N = 5, 5, 4, respectively. The measured observed fluxes are reported in Table 1. These correspond to relative ratios of $1 : 1.0^{+0.5}_{-0.3} : 0.87^{+0.47}_{-0.36}$ for λ8498:λ8542:λ8662 w.r.t λ8498. This is close to the ratios derived for I Zw 1 by R. J. Rudy et al. (2000). The photon flux ratio for the Ca II multiplet and the O I λ8446 ($ROI_{Ca\,II}$), assuming a representative wavelength of 8579Å, is $ROI_{Ca\,II} = 0.62^{+0.16}_{-0.12}$.

Fe II emission lines. As shown in the right panel of Figure 3, in the UV the Vestergaard's template seems to properly model the blend of Mg II and Fe II at $\lambda_{rest} = 2800$Å, and it reproduces the spectral shape at 2200Å $\lesssim \lambda_{rest} \lesssim$ 2600Å. However, the observed flux intensity of the Fe II lines in the 2200Å $\lesssim \lambda_{rest} \lesssim$ 2600Å regime is not well described by the template. This discrepancy is partially solved when varying the flux ratios of the Fe II emission in 2200Å $\lesssim \lambda_{rest} \lesssim$ 2600Å compared to the Fe II emission around Mg II (see Appendix C and I. Labbe et al. 2024). The variation of intrinsic flux ratios implies that the observed gas conditions differ from those assumed in the template model (M. Vestergaard & B. J. Wilkes 2001), but it is difficult to draw strong conclusions based on the poor resolution of the available data.

Given the known discrepancies between iron templates, we also tried to fit Fe II in the UV using the Fe II template from Y. Tsuzuki et al. (2006). Results are reported in detail in Appendix C. Unlike the Vestergaard's template where Mg II is masked, Y. Tsuzuki et al. (2006) also model the Fe II emission beneath and blended with Mg II. Unfortunately, the low spectral resolution of the data prevents us from appreciating these differences between the templates. Indeed, the quality of the fit using Vestergaard's or Tsuzuki's template is the same.

Alternatively, we modeled the UV Fe II emission with HOMERUN (A. Marconi et al. 2024), a multi-cloud photoionization framework that fits observed line fluxes as a non-negative combination of CLOUDY models (see Appendix C for details). The resulting Fe II template (no turbulence) reproduces the emission around Mg II but fails to match the ∼ 2500 Å bump; single-cloud models with turbulence recover this feature, but disagree with constraints from other lines. This tension points to including turbulence in HOMERUN, testing ad-hoc ionizing continua for AGN LRDs, and ultimately doing full-spectrum fitting of the Fe II pseudo-continuum — steps we leave for future work.

In the optical, the Fe II lines are well modeled by a single Gaussian, but are all unresolved at the spectral resolution of the prism (see left panel of Figure 3).

4. DISCUSSION

4.1. *Evidence for the broad-line region stratification*

The detection of iron emission in the UV and in the optical gives us unambiguous evidence of an AGN (see Sect. 1). This is further corroborated by the detection of the O I and Ca II lines and the broad Hα emission. Although we are unable to spectrally resolve —and thus model in detail — the iron multiplets in the UV, the detection of the iron signatures across the spectrum supports a scenario in which emission lines throughout the spectrum arise from the BLR, photoionized by the central BH (see also discussion in I. Labbe et al. 2024).

In cases like Bz5.3 with poor spectral resolution, there is a current debate whether these features arises from the broad emitting region or the narrower one, i.e. if these are broad permitted emission lines (I. Labbe et al. 2024; J. Kovačević-Dojčinović et al. 2025), or narrow forbidden ones (X. Lin et al. 2025).

Following the first interpretation, in the optical we detect two categories of Fe II emission lines. Fe II λ4278 is classified as an 'inconsistent' Fe II line, while Fe II λ5165, Fe II λ5274 and Fe II λ5335 as 'consistent' ones. The appearance of lines that should be negligible based on their transition probabilities, namely 'inconsistent' lines, has been recently studied and classified by J. Kovačević-Dojčinović et al. (2025). Based on the reported classification, Fe II λ4278 belongs to the P+ group of 'inconsistent' lines. These are thought to arise either from lines from higher energy levels at similar wavelengths overlapping with these weak lines or from the same levels as consistent lines but amplified by unknown atomic processes. The presence and strength of 'inconsistent' emission lines is known to increase for $FWHM_{Fe\,II,opt} < 5000$ km s^{-1}. In the case of Bz5.3, the prism resolution limits the measured FWHM to be $\lesssim 1800$ km s^{-1} in the optical and $\lesssim 3000$ km s^{-1} in the UV, consistent with this trend. The diversity in both intensity, and possibly widths, among the consistent and inconsistent lines suggests that they originate from regions with varying physical conditions and distances from the BH, indicating a stratification of the Fe II emitting regions, and thus of the BLR (J. Kovačević-Dojčinović et al. 2025).

The more stringent constraint on their line widths ($FWHM_{Fe\,II,opt} \lesssim 1800$ km s^{-1}) favours the second interpretation for the nature of the optical iron features. Indeed, [Fe II] have been recently detected and modeled in two local LRDs by X. Lin et al. (2025). Based on the comparison with photoionization models and the FWHM of [Fe II] (∼ 200 − 300 km s^{-1}), they propose the [Fe II]-emitting region to lie right at the edge of the BLR, supporting the view of a stratified inner region, and just outside the cool gas envelope. For Bz5.3 the presence of the cool-gas envelope can

be supported by the evidence of the Balmer break, given that Balmer absorption features, if present, are not detectable at the current resolution.

Finally, the difference in line widths between LILs and Balmer lines further supports the picture of a stratified BLR, although the resolution of the prism can only set upper limits for most LIL line widths. Specifically, for the Balmer lines, we derived $\mathrm{FWHM}_{\mathrm{H}\alpha} = 4600 \pm 50$ km s^{-1} and $\mathrm{FWHM}_{\mathrm{H}\beta} = 5100 \pm 500$ km s^{-1}, while for the LILs we reported $\mathrm{FWHM}_{\mathrm{Fe\,II,UV}} \lesssim 3000$ km s^{-1}, $\mathrm{FWHM}_{\mathrm{Fe\,II,opt}} \lesssim 1800$ km s^{-1}, $\mathrm{FWHM}_{\mathrm{O\,I}\lambda 8446} = 940^{+50}_{-100}$ km s^{-1}, $\mathrm{FWHM}_{\mathrm{Ca\,II}} \lesssim 900$ km s^{-1}. LIL line widths differ by 2-3 thousands km s^{-1} from the Balmer lines, implying that the LIL-emitting region is farther away from the central source in the BLR.

As briefly stated in Sect. 1, there seems to be a link between BLR tracers and LRDs, possibly due to BH properties or geometric effects. We note that both LRDs with robust Fe II detection, Bz5.3 and A2744-45924, have a low Eddington ratio ($\lambda_{\mathrm{Edd,Bz5.3}} = 0.010^{+0.020}_{-0.007}$, and $\lambda_{\mathrm{Edd,A2744}} < 0.03$, from X. Ji et al. 2025; L. J. Furtak et al. 2024; I. Juodžbalis et al. 2025). However, if black-hole masses from single-epoch virial calibrations are to be trusted, this seems to be in contrast to many studies reporting a correlation between Fe II strength and Eddington ratio (J. Kovačević-Dojčinović et al. 2025; J. W. Sulentic et al. 2000; Y. Shen & L. C. Ho 2014; M. Gaskell et al. 2022; M. L. Martínez-Aldama et al. 2021). In contrast, if we believe mass estimates from the electron-scattering scenarios, then most AGN LRDs would be super-Eddington (or even highly super-Eddington, in the quasi-star model). As for the current state of the models and observations available, the origin of this link remains an open question.

4.2. *Dust attenuation and origin of UV continuum*

According to the Grotrian diagram[8] for O I (see e.g. Figure 3 in S. A. Grandi 1980), the ROI of λ1304/λ8446 ($\mathrm{ROI_{UV}}$) must be equal to unity, in principle only decreasing when reddening is present. This is why the photon flux ratio between λ1304 and λ8446 has been used as reddening indicator (e.g., R. J. Rudy et al. 1989; A. Laor et al. 1997; A. Rodríguez-Ardila et al. 2002; Y. Matsuoka et al. 2005). These works also suggest that the $\mathrm{ROI_{UV}}$ can deviate from unity[9], down to 0.63 even in the absence of reddening. This could be due to (i) Balmer continuum absorption of λ1304 photons, or (ii) the production of λ8446 by collisional excitation, or (iii) by collisional de-excitation destroying λ1304 photons (J. Kwan & J. H. Krolik 1981; S. A. Grandi 1980). For Bz5.3, we estimated an $\mathrm{ROI_{UV}}$ between 0.1 and 0.3 (see Sect. 3.3) therefore, even if the λ1304 is severely affected by destruction mechanisms or the λ8446 is pumped by collisional excitation, these mechanisms are not sufficient to explain such a break of the one-to-one photon relation between λ8446 and λ1304 (as also discussed in A. Rodríguez-Ardila et al. 2002). Since we do observe a Balmer break in Bz5.3, and since these features have been associated with dense gas near AGN (K. Inayoshi & R. Maiolino 2025; X. Ji et al. 2025; R. P. Naidu et al. 2025; A. de Graaff et al. 2025), a discussion of Balmer-continuum absorption is warranted. Comparing Bz5.3 to A2744-45924 (see Figure 1) reveals that our AGN has a weaker break and steeper UV slope. This implies that Balmer absorption near λ1304 may not be dominant, since the weak break compounds the decreasing bound-free cross section blueward of the Balmer limit. Independent evidence for weak neutral-gas absorption comes from the sharpness of the Lyα break in Bz5.3, suggesting that the UV photons propagate through a path largely free of neutral hydrogen, which would otherwise leave a spectral-absorption imprint, as seen in the smooth Lyα break of A2744-45924. Thus, we favour dust playing a major role in altering the observed O I ratio.

We derive $E(B-V)$ and the dust attenuation (A_V) considering the observed $\mathrm{ROI_{UV}}$ derived in Sect. 3.3, both the intrinsic $\mathrm{ROI_{UV}}$ presented above, and assuming the Calzetti law for the dust attenuation curve (D. Calzetti et al. 1996). Results are reported in Table 2. We also consider the limit case of having a fraction of O I λ1304 of 20%. Our findings point toward relatively high values of dust attenuation in the BLR, ranging from 0.4 to 1.4.

To assess the origin of the continuum under the O I λ1304 line, we use the range of derived dust attenuation to correct the observed UV β slope, $\beta_{\mathrm{UV}} = -1.6 \pm 0.1$. Assuming $A_V \in [0.4, 1.0]$, we obtain intrinsic UV beta slopes of $\beta_{\mathrm{UV,int}} = [-2.8, -2.0]$. This is broadly consistent with a standard accretion disk (i.e. $\beta = -2.3$, see N. I. Shakura & R. A. Sunyaev 1976), and towards the steepest end with extreme star formation. Similar steep intrinsic UV slopes have been recently found both in the local LRDs at $z \sim 0.1 - 0.2$ (X. Lin et al. 2025), and in LRDs at $z > 4$ (see e.g. I. Labbe et al. 2024; R. Tripodi et al. 2024). These works favor the interpretation of the UV being dominated by AGN light, also motivated by the high EW of the UV emission lines.

4.3. *Insights from the Ca II transitions*

Comparisons of the Ca II triplet with Hβ and Fe II feature strengths could better constrain BLR properties and geometry. However, such analysis is hindered by: (1) the limited resolution of the prism, which prevents detailed modeling of UV Fe II emission; and (2) large uncertainties in de-reddened line fluxes due to the variable dust attenuation inferred from

[8] A Grotrian diagram, or term diagram, shows the allowed electronic transitions between the energy levels of atoms. They can be used for one-electron and multi-electron atoms.

[9] Values of $\mathrm{ROI_{UV}} = 1$ and $= 0.63$ corresponds to intrinsic flux ratios of 6.5 and 4, respectively.

Table 2. $E(B-V)$ and dust attenuation from the O I lines

	$ROI_{UV,int}$ = 1.0			$ROI_{UV,int}$ = 0.63		
	no Si II	50% Si II (fiducial)	80% Si II	no Si II	50% Si II (fiducial)	80% Si II
$E(B-V)$	0.16 ± 0.04	0.24 ± 0.04	0.36 ± 0.05	0.10 ± 0.04	0.19 ± 0.04	0.30 ± 0.05
A_V	0.65 ± 0.20	1.0 ± 0.2	1.4 ± 0.2	0.42 ± 0.20	0.80 ± 0.20	1.2 ± 0.2

Notes. The columns specify the assumptions made to compute the values of dust attenuation.

the O I λ1304/λ8446 ratio. Estimating attenuation from the broad Balmer lines is even more uncertain due to blending with nearby features (e.g., [O III]λ5007, [O III]λ4364, Fe II) at the current resolution.

The near-unity relative strengths of the Ca II λ8498,8542,8662 lines suggest they are optically thick (G. J. Ferland & S. E. Persson 1989), consistent with the redshift in their centroids (Figure 2), as expected from resonant scattering. Other Ca II lines—such as H, K, and the forbidden λ7291 and λ7324 Å —are typically absent in AGNs (G. J. Ferland & S. E. Persson 1989) and are also undetected in Bz5.3. The Ca II λ8498,8542,8662/O I λ8446 flux ratio varies across AGNs but is generally near unity (minimum 0.35 ± 0.19; G. J. Ferland & S. E. Persson 1989); for Bz5.3, we find $0.61^{+0.15}_{-0.12}$, consistent with this range.

4.4. *Excitation mechanisms in the BLR*

If Lyβ fluorescence is the dominant excitation mechanism, the O I transitions at λ1304, λ8446, and λ11287 should appear in a 1:1:1 photon flux ratio. However, this ratio can be altered by three competing processes: recombination, collisional excitation, and continuum fluorescence. The presence or absence of auxiliary O I lines such as λ7774 and λ7990 provides diagnostic power to identify the dominant mechanisms (see Sect. 1; S. A. Grandi 1980; H. Landt et al. 2008; Y. Matsuoka et al. 2005, 2007, 2008).

Lyβ fluorescence and collisional excitation are the main sources of O I λ8446 emission in the BLR. S. A. Grandi (1980) first identified the absence of a narrow O I λ8446 component — supporting a BLR origin — and proposed Lyβ fluorescence as the dominant mechanism, later confirmed by the 1:1:1 line ratio in I Zw 1 (R. J. Rudy et al. 1989). Subsequent studies showed collisional excitation is also significant (A. Rodríguez-Ardila et al. 2002; H. Landt et al. 2008), while continuum fluorescence plays a minor role. Photoionization models by Y. Matsuoka et al. (2007) showed both mechanisms operate efficiently in gas with $n_{\rm H} \sim 10^{11.5}$ cm^{-3} and $\log(U) \sim -2.5$.

In Bz5.3, we clearly detect O I λ8446, Ca II λ8498,8542,8662 triplet and we have upper limits on O I λ7774 and O I λ7990. Consistent with a BLR origin, O I λ8446 exhibits broad emission (see Table 1), though it is several thousand km s^{-1} narrower than the broad Balmer lines—supporting the notion of a stratified BLR. In agreement with the aforementioned studies in local AGNs, for Bz5.3, Lyβ fluorescence is the main production mechanism of LILs based on the following evidence. (1) The high equivalent width of O I λ8446 can be explained only in the presence of Lyβ pumping the production of O I λ8446 photons. Indeed, it has been shown that in the presence of mechanisms hampering the Lyβ fluorescence efficiency, e.g. turbulent gas, the EW of O I λ8446 decreases to < 10Å (Y. Matsuoka et al. 2007; M. Bottorff et al. 2000). (2) The weakness of the O I λ7774,λ7990 emission lines compared to O I λ8446. Indeed their flux ratios are expected to be > 1 for pure recombination, while O I λ7774,λ7990 are just a few percents of O I λ8446 (< 10 − 20%) in case of a combination of Lyβ fluorescence and collisional excitation (Y. Matsuoka et al. 2007).

Indeed, we also observe the presence of other competing mechanisms given that the O I λ1304/λ8446 photon flux ratio is much lower than unity. We can rule out recombination as a player in fostering the production of LILs, since O I λ7774/λ8446 < 0.23 (O I λ7774/λ8446 ∼ 1.1 for recombination). Instead, this flux ratio is close to the expected one for collisional excitation (0.3, see Y. Matsuoka et al. 2007). In contrast, the O I λ7990/λ8446 ratio of < 0.28 is rather uninformative, since it is expected to be ∼ 0.05 for continuum fluorescence (S. A. Grandi 1980).

We can rule out continuum fluorescence given that EW(O I λ8446)= 24 ± 2 Å, while EW(O I λ8446)≤ 1 Å is expected (Y. Matsuoka et al. 2007). This high equivalent width also supports the role of collisional excitation, which is more effective for higher EW(O I λ8446) that implies higher densities (Y. Matsuoka et al. 2007).

The contribution from scattered light is also ruled out, since we would expect much higher O I λ1304/λ8446 ratio than observed, roughly proportional to the scattered fraction.

The complexity of the BLR in LRD is highlighted by comparing the results for the EW(O I λ8446) and $ROI_{\rm Ca\,II}$ with simple photo-ionization models. In particular, we use the models provided in Y. Matsuoka et al. (2007), who performed a similar analysis for QSOs at $z < 1$. The BLR gas in their work was modeled to have a constant hydrogen density and exposed to the ionizing continuum radiation with varying photon flux, Φ, connected to the ionization parameter as $U \equiv \Phi/(n_{\rm H}c)$ where c is the speed of light. They performed calculations with $(n_{\rm H}, U)$ sets in a range of $10^7 \leq n_{\rm H} \leq 10^{14}$ cm^{-3}, and $10^{-5} \leq U \leq 10^0$, stepped by 0.5 dex. They have a BLR gas with $N_{\rm H} = 10^{23}$ cm^{-2} and

$v_{\rm turb} = 0$ km s^{-1}, where $N_{\rm H}$ is the column density and $v_{\rm turb}$ is the microturbulent velocity. We do not consider other models presented in their work with higher $v_{\rm turb}$ values, since they imply EW(O Iλ8446)$\leq$ 10 Å, in contrast with our observations. Therefore, based on their 'standard' model and the observed EW(O Iλ8446) and ROI$_{\rm Ca\,II}$ for Bz5.3, we find that $-4 < \log(U) < -3.5$, and $n_{\rm H} \sim 10^{9.5}$ cm^{-3} (see Figure 7 in Y. Matsuoka et al. 2007). However, other models favour higher densities and ionization to reproduce Fe II emission in local AGNs ($\log(n_{\rm H}/{\rm cm}^{-3}) \sim 10 - 11$, $\log(U) \sim -2.5$, e.g. X. Lin et al. 2025). A step forward would be to generate tailored models to reproduce the observed complex stratification observed in the BLR taking into account constraints from Fe II emission, which is however beyond the scope of this Letter (see e.g., X. Lin et al. 2025; S. Panda et al. 2020; D. Dias dos Santos et al. 2024).

5. SUMMARY AND CONCLUSIONS

In this work, we present a spectroscopic study of BLR LIL diagnostics in Bz5.3, a $z = 5.3$ AGN host galaxy, based on *JWST*/NIRCam and NIRSpec observations covering rest-frame UV to optical wavelengths. Our main conclusions are as follows:

- The detection of Fe II, λ1304 bump, broad O I, and Ca II triplet emission lines supports the presence of a BLR and thus an AGN in Bz5.3, already suggested by evidence of broad Balmer emission.
- We report the first detection of the λ1304 bump at $z > 5$, a key spectral signature of the BLR previously seen only in local AGN. This detection extend the study of local diagnostics of the BLR physical conditions to $z > 5$.
- While the iron features in Bz5.3 may arise from either broad permitted or narrow forbidden transitions, the diversity in line strengths and widths—along with their consistency with recent models—supports the presence of physically distinct emitting regions. Regardless of the interpretation, the observed iron emission points to a stratified BLR.
- Excitation diagnostics suggest that Lyβ fluorescence is the primary mechanism powering the O I lines, particularly O Iλ8446, with collisional excitation also contributing. Recombination and continuum fluorescence are disfavored based on upper limits on O Iλ7774 and O Iλ7990, and the large equivalent width of O Iλ8446 (24 ± 2 Å).
- The photon flux ratio O Iλ1304/λ8446 is significantly below unity (0.1–0.3), pointing to substantial dust attenuation within the BLR. We derive $A_V \sim 0.4$–1.4 based on these ratios. We disfavour bound-free absorption since the weak break compounds the decreasing bound-free cross section blue-ward of the Balmer limit.
- The Ca II triplet shows nearly equal line ratios, indicating optically thick conditions. This observation is consistent with an observed redshift of the line centroid, as expected from resonant scattering. The measured Ca II/O Iλ8446 flux ratio ($\sim$ 0.6) is consistent with low-redshift AGNs, further supporting a BLR origin for these lines.
- Comparison with photoionization models suggests that the observed O Iλ8446 and ROI$_{\rm Ca\,II}$ features in Bz5.3 are best reproduced by a low-ionization, high-density BLR component, distinct from the conditions typically required for iron emission. This apparent tension further supports a stratified BLR structure, with multiple gas phases coexisting under different physical conditions—underscoring the need for tailored models to capture this complexity.

A detailed study of the BLR through LIL diagnostics such as Fe II, O I and Ca II, have usually been limited to the low-z Universe ($z < 1$), mainly due to a combination of poor resolution and sensitivity. This is especially true for O Iλ1304, which is usually faint and often blended with Lyα emission or hidden by Lyα damping wings (see e.g., I. Labbe et al. 2024). Taken together, our findings provide a rare and detailed glimpse into BLR conditions in LRDs at early times, demonstrating the power of *JWST* spectroscopy in probing AGN physics in the early Universe. Nonetheless, the limited resolution of the NIRSpec prism restricts a robust analysis of LILs and the BLR structure, motivating follow-up observations with higher-resolution spectroscopy.

While extending this analysis to a large population of high-redshift galaxies remains challenging — particularly for the faint and blended O Iλ1304 bump — targeted, deep observation of carefully selected sources offers a promising path forward for probing the structure and physics of the BLR in the early Universe. In parallel, the recent discovery of local LRD analogs provides a valuable laboratory for investigating BLR properties in greater detail. Tailored UV spectroscopic follow-up with instruments like HST/COS for local LRDs and JWST/NIRSpec gratings for high-z ones will be essential for bridging the gap between low- and high-redshift LRDs, enabling a more complete picture of BLR excitation mechanisms and evolution over cosmic time.

Data Avalability: all the *JWST* data used in this paper can be found in MAST: 10.17909/2hxk-5h89.

ACKNOWLEDGEMENTS

We thank Dr. Marianne Vestergaard and Dr. Yoshiki Matsuoka for kindly sharing the iron templates used in this work and their insightful suggestions. The authors also thank Dr. Cupani and Dr. Calderone for their useful suggestions on the use of iron templates. RT, MB, NM, VM, AH, GR, JJ, and GF acknowledge support from the ERC Grant FIRSTLIGHT and from the Slovenian national research agency ARIS through grants N1-0238 and P1-0188. GR and MB acknowledge support from the European Space Agency through Prodex Experiment Arrangement No. 4000146646. This research was enabled by grant 18JWST-GTO1 from the Canadian Space Agency, and Discovery Grants from the Natural Sciences and Engineering Research Council of Canada to MS, RA, and AM. This research used the Canadian Advanced Network For Astronomy Research (CANFAR) operated in partnership by the Canadian Astronomy Data Centre and The Digital Research Alliance of Canada with support from the National Research Council of Canada, the Canadian Space Agency, CANARIE and the Canadian Foundation for Innovation. This work is based on observations made with the NASA/ESA/CSA James Webb Space Telescope. The data were obtained from the Mikulski Archive for Space Telescopes at the Space Telescope Science Institute, which is operated by the Association of Universities for Research in Astronomy, Inc., under NASA contract NAS 5-03127 for JWST. These observations are associated with program #4598. Support for program #4598 was provided by NASA through a grant from the Space Telescope Science Institute, which is operated by the Association of Universities for Research in Astronomy, Inc., under NASA contract NAS 5-03127. BL is supported by the international Gemini Observatory, a program of NSF NOIRLab, which is managed by the Association of Universities for Research in Astronomy (AURA) under a cooperative agreement with the U.S. National Science Foundation, on behalf of the Gemini partnership of Argentina, Brazil, Canada, Chile, the Republic of Korea, and the United States of America.

APPENDIX

A. GALFIT FIT

In the left panel of Figure 4, we show the results of the `Galfit` modeling of Bz5.3 with a point source. We find strong residuals in all filters except F410M and F444W, where the source is unresolved and fully consistent with a point source. Therefore, we add an additional component for all the filters at $\lambda < 4\ \mu m$ in the form of a Sérsic profile with varying index n and half-light radius R_e. As shown in the right panel of Figure 4, this setup produces goods results with few residuals.

B. DETAILS ON THE SPECTRAL FITTING PROCEDURE

Regarding the fit of the spectral features reported in Sect. 3.1, we explore the parameter space with a Markov chain Monte Carlo (MCMC) algorithm implemented in the `EMCEE` package, assuming uniform priors for slopes, normalizations, and FWHM of the Gaussian. Priors on the FWHM of narrow lines are tight, taking into account the known varying resolution with wavelength of the prism. We consider $\mathrm{FWHM_{prior}} \in [0.8, 1.2]$ spectral resolution element, whose size vary with wavelength. The prior on the peak wavelength is Gaussian, centered on $z_{\mathrm{source}} = 5.2907$, and with $\sigma = 10$Å, corresponding to the best spectral resolution achieved in the spectrum at the source's redshift. We consider 10 walkers per parameter and 2500 trials, with a typical burn-in phase of ~ 300 trials.

We compute the integrated line fluxes by integrating the best-fitting functions for each emission line, which are quoted as the 50th percentile, and we derive the error from the 16th and 84th percentiles. Upper or lower limits are given at 3σ. When measuring line widths, an additional complication is given by the instrumental broadening effect by the detector line spread function (LSF), which can be approximated as a Gaussian profile of a certain FWHM (P. Jakobsen et al. 2022). Therefore, we report de-convolved FWHM computed via $\mathrm{FWHM_{dec}} = \sqrt{\mathrm{FWHM^2_{obs}} - \mathrm{FWHM^2_{LSF}}}$ relation, where $\mathrm{FWHM_{obs}}$ and $\mathrm{FWHM_{LSF}}$ are the observed and instrumental FWHM (publicly available in the JWST website), respectively. We mention that LSF correction are usually negligible for broad lines in the rest-frame optical regime, e.g. > 10 times wider than the $\mathrm{FWHM_{LSF}}$. FWHM below the spectral resolution of the instrument are not reported. We measure the EW of emission lines for each trial in the chain. Then, we derive the best-fitting value from the 50th percentile of the EW's chain, and the error on EW from the 16th and 84th percentiles.

C. ALTERNATIVE Fe II AND Mg II FITS

As shown in the bottom panel of Figure 3 and in Sect. 3.3, the template from M. Vestergaard & B. J. Wilkes (2001) are able to reproduce the overall shape of the Fe II emission in $2200\text{Å} \lesssim \lambda_{\mathrm{rest}} \lesssim 2600\text{Å}$, however the flux ratios of the Fe II transitions assumed in the template differ from the observed ones in Bz5.3. Therefore, to allow more flexibility in the model, we splitted the template

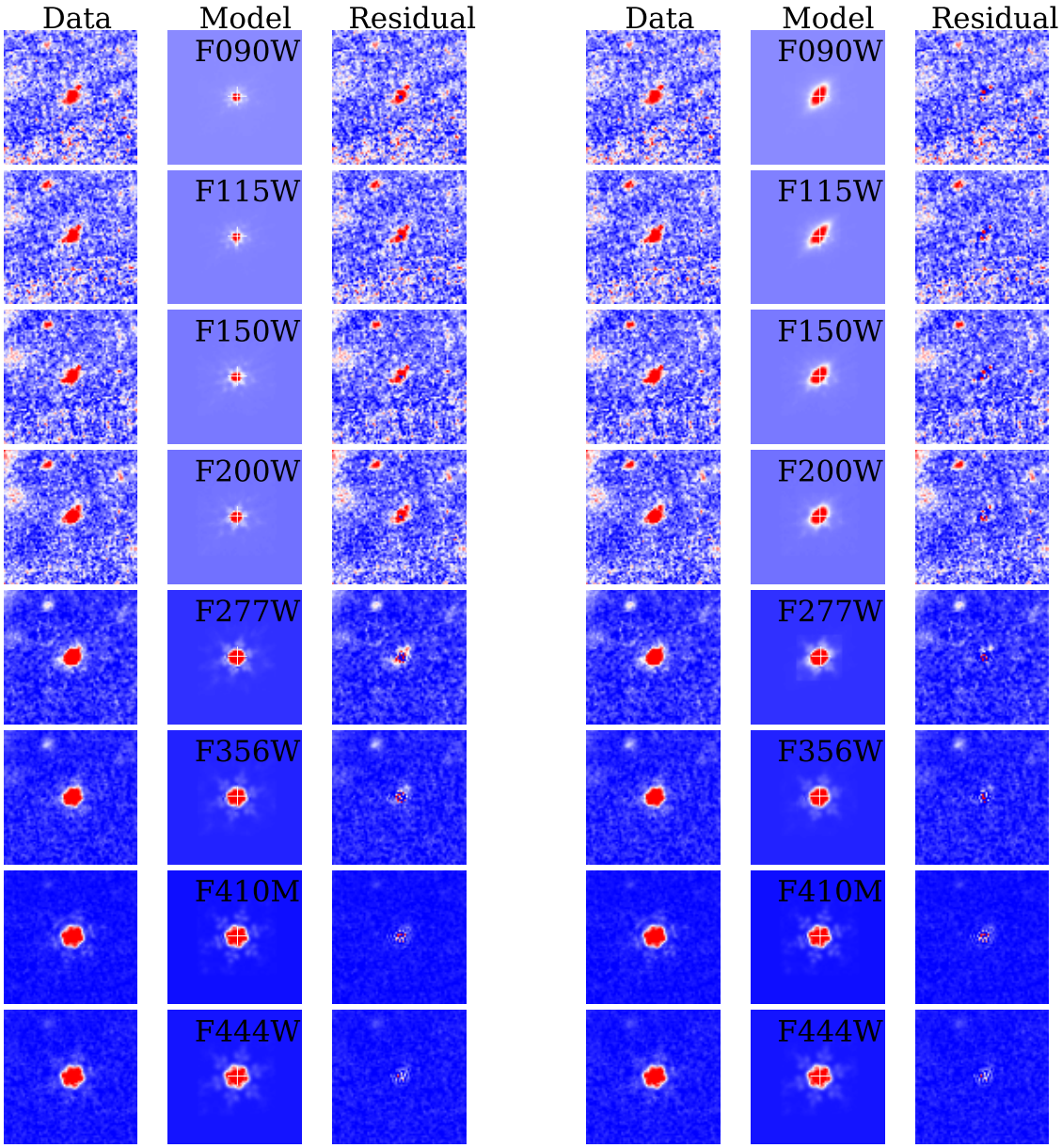

Figure 4. Results of modeling Bz5.3 with `Galfit`. Left panels: data and results assuming a single point source as model for each filter. The white cross indicates the centroid of the model. Right panels: data and results assuming as model a combination of a point source and a Sérsic profile for each filter with $\lambda < 4\ \mu m$, a single point source otherwise.

into two sections separated at $\lambda_{\rm rest} = 2700$Å, isolating the Mg II emission region from the rest of the Fe II pseudo-continuum. We show the results in Figure 5. The fit is now much closer to the observed data at $\lambda_{\rm rest} < 2700$Å, as shown by the lower reduced χ^2 value compared to the previous fit. This implies that a proper modeling of the Fe II emission would require higher resolution data to better resolve the pseudo-continuum followed by templates with different assumptions for the gas conditions.

Alternatively, given the known discrepancies with Fe II templates, we run an analogous fit using the template from Y. Tsuzuki et al. (2006). As shown in Figure 6, we obtained a similar result as when using Vestergaard's template. Indeed, the low resolution of the data in the UV regime prevents us from distinguishing between different models of Fe II emission.

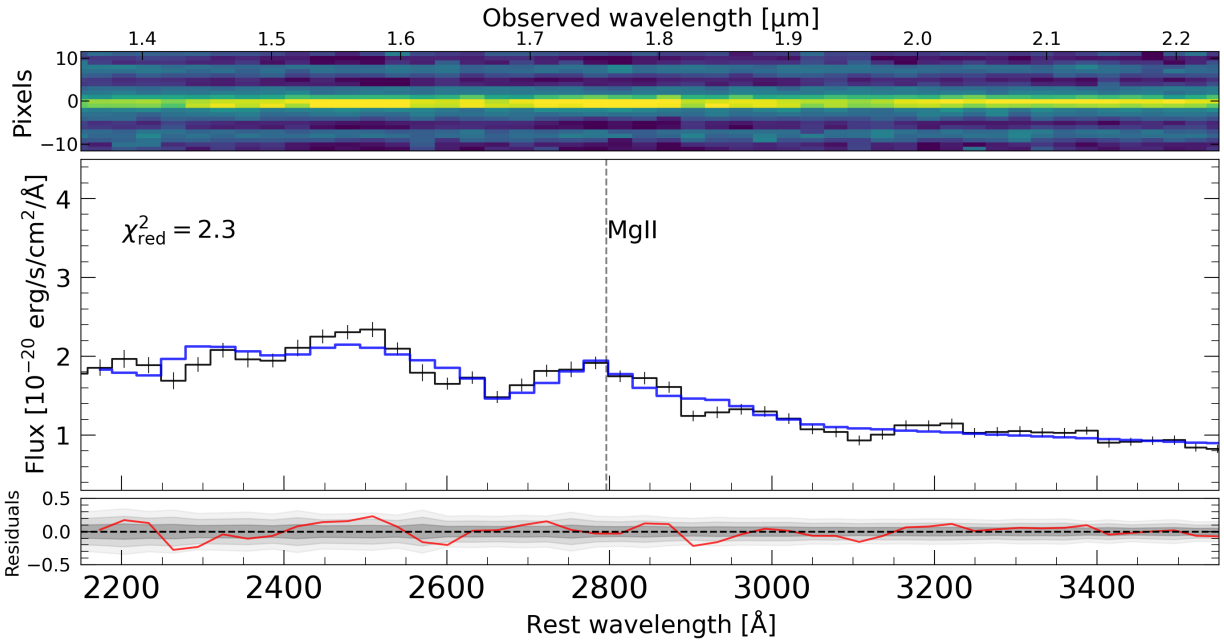

Figure 5. Zoom-in of the 2D and 1D spectra of Bz5.3 on the Fe II complex in the UV and Mg II emission line. The observed spectrum is shown in black, while the best-fitting model is shown in blue. Residuals are shown at the bottom of each panel, where the shaded dark gray area represents the 1σ noise level. 2 and 3σ noise levels are reported in the residual as shaded lighter gray area.

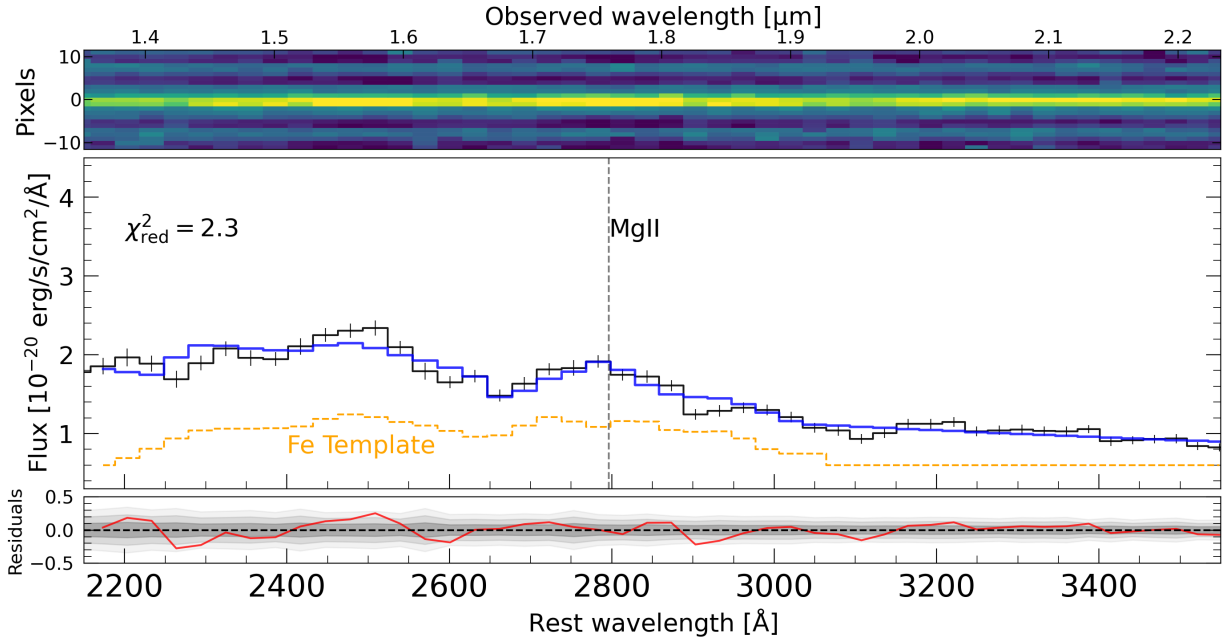

Figure 6. Same as Figure 5 but for Tsuzuki's template (shown in yellow).

Seeking a more reliable match to the UV Fe II emission, we adopted a tailored photoionization model for the observed data. Specifically, we modeled the emission lines listed in Table 1, together with C III], C IV, and the broad components of Hα and Hβ, using HOMERUN (A. Marconi et al. 2024; M. Ceci et al. 2025). HOMERUN (Highly Optimized Multi-cloud Emission-line Ratios Using photoionizatioN; A. Marconi et al. 2024) is a multi-cloud photoionization framework in which the observed emission lines are reproduced as a weighted linear combination of constant-density CLOUDY models, each characterized by a specific ionizing photon flux and density but sharing the same ionizing spectrum and chemical composition. The key innovation is that the weights are treated as free parameters and determined by fitting the observed line fluxes to the model predictions via

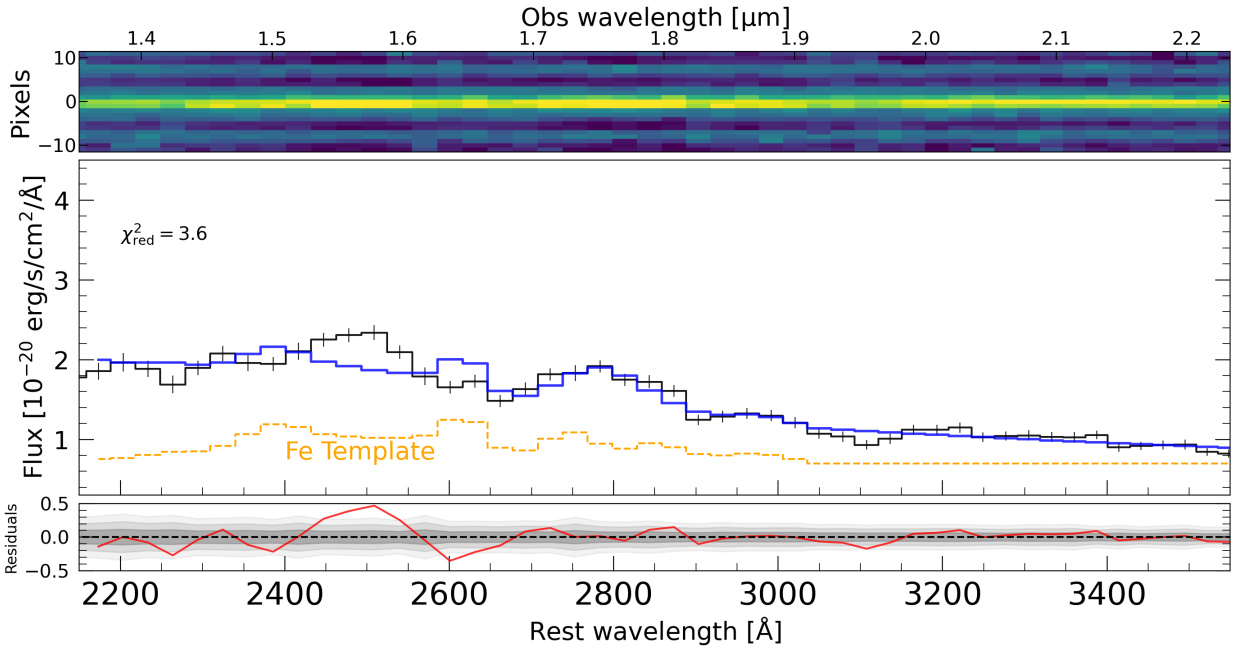

Figure 7. Same as Figure 5 but for the HOMERUN template (shown in yellow).

non-negative least-squares minimization. From the HOMERUN best-fit model, we inferred the combination of gas densities and ionizing photon fluxes consistent with our observations (specifically,[10] $\log(\bar{n}) = 10.9$, $\log(\bar{\phi}) = 17.7$). We then computed synthetic Fe II templates with CLOUDY v23.01 (C. M. Gunasekera et al. 2023), adopting the table AGN ionizing continuum (W. G. Mathews & G. J. Ferland 1987) and matching the metallicity to the HOMERUN best-fit value ($12 + \log(\mathrm{O/H}) = 7.8$). To ensure that all relevant atomic levels and transitions were included, we used the full Fe II model atom implemented in CLOUDY, based on the Stout database (G. J. Ferland & S. E. Persson 1989) with updated atomic data from R. T. Smyth et al. (2019). No turbulence was included, consistent with the HOMERUN best-fit model. The resulting template and its fit to our data are shown in Fig. 7. While the new template reproduces the observed Fe II emission around Mg II well, it fails to recover the ~ 2500 Å bump, unlike the templates by (M. Vestergaard & B. J. Wilkes 2001) and (Y. Tsuzuki et al. 2006). Given the strong sensitivity of Fe II emission to gas turbulence, we also tested simpler single-cloud models with non-zero turbulence, which reproduce the ~ 2500 Å bump but are inconsistent with the observed fluxes of other lines. A natural step forward would be to investigate the effects of including non-zero turbulence in HOMERUN, as well as building 'ad hoc' ionizing continuum shapes for AGN LRDs. Moreover, a proper treatment of Fe II pseudo-continuum would require a full-spectrum fitting, which is not implemented in the current version of HOMERUN. While it would be a natural extension of the code, this is beyond the scope of this paper.

REFERENCES

Ananna, T. T., Bogdán, Á., Kovács, O. E., Natarajan, P., & Hickox, R. C. 2024, ApJL, 969, L18, doi: 10.3847/2041-8213/ad5669

Baldwin, J. A., Ferland, G. J., Korista, K. T., Hamann, F., & LaCluyzé, A. 2004, ApJ, 615, 610, doi: 10.1086/424683

Bottorff, M., Ferland, G., Baldwin, J., & Korista, K. 2000, ApJ, 542, 644, doi: 10.1086/317051

Brammer, G. 2019, Grizli: Grism redshift and line analysis software,, Astrophysics Source Code Library, record ascl:1905.001

Calzetti, D., Kinney, A. L., & Storchi-Bergmann, T. 1996, ApJ, 458, 132, doi: 10.1086/176797

Ceci, M., Marconcini, C., Marconi, A., et al. 2025, arXiv e-prints, arXiv:2507.08077, doi: 10.48550/arXiv.2507.08077

Cha, S., Cho, B. Y., Joo, H., et al. 2025, ApJL, 987, L15, doi: 10.3847/2041-8213/add2f0

Clowe, D., Bradač, M., Gonzalez, A. H., et al. 2006, ApJL, 648, L109, doi: 10.1086/508162

de Graaff, A., Rix, H.-W., Naidu, R. P., et al. 2025, arXiv e-prints, arXiv:2503.16600, doi: 10.48550/arXiv.2503.16600

Dias dos Santos, D., Panda, S., Rodríguez-Ardila, A., & Marinello, M. 2024, Physics, 6, 177, doi: 10.3390/physics6010013

[10] The barred quantities are the harmonic means of the gas density and ionizing photon flux, respectively.

Dong, X.-B., Wang, T.-G., Wang, J.-G., et al. 2009, ApJL, 703, L1, doi: 10.1088/0004-637X/703/1/L1

Espey, B. R., Carswell, R. F., Bailey, J. A., Smith, M. G., & Ward, M. J. 1989, ApJ, 342, 666, doi: 10.1086/167627

Ferland, G. J., Done, C., Jin, C., Landt, H., & Ward, M. J. 2020, MNRAS, 494, 5917, doi: 10.1093/mnras/staa1207

Ferland, G. J., & Persson, S. E. 1989, ApJ, 347, 656, doi: 10.1086/168156

Furtak, L. J., Labbé, I., Zitrin, A., et al. 2024, Nature, 628, 57, doi: 10.1038/s41586-024-07184-8

Gaskell, M., Thakur, N., Tian, B., & Saravanan, A. 2022, Astronomische Nachrichten, 343, e210112, doi: 10.1002/asna.20210112

Grandi, S. A. 1980, ApJ, 238, 10, doi: 10.1086/157952

Greene, J. E., & Ho, L. C. 2005, ApJ, 630, 122, doi: 10.1086/431897

Grier, C. J., Martini, P., Watson, L. C., et al. 2013, ApJ, 773, 90, doi: 10.1088/0004-637X/773/2/90

Guarcello, M. G., Drake, J. J., Wright, N. J., García-Alvarez, D., & Kraemer, K. E. 2014, ApJ, 793, 56, doi: 10.1088/0004-637X/793/1/56

Gunasekera, C. M., van Hoof, P. A. M., Chatzikos, M., & Ferland, G. J. 2023, Research Notes of the American Astronomical Society, 7, 246, doi: 10.3847/2515-5172/ad0e75

Hamann, F., & Ferland, G. 1993, ApJ, 418, 11, doi: 10.1086/173366

Hamann, F., & Ferland, G. 1999, ARA&A, 37, 487, doi: 10.1146/annurev.astro.37.1.487

Inayoshi, K., & Maiolino, R. 2025, ApJL, 980, L27, doi: 10.3847/2041-8213/adaebd

Jakobsen, P., Ferruit, P., Alves de Oliveira, C., et al. 2022, A&A, 661, A80, doi: 10.1051/0004-6361/202142663

Ji, X., Maiolino, R., Übler, H., et al. 2025, arXiv e-prints, arXiv:2501.13082, doi: 10.48550/arXiv.2501.13082

Joly, M. 1987, A&A, 184, 33

Joly, M. 1989, A&A, 208, 47

Jullo, E., & Kneib, J. P. 2009, MNRAS, 395, 1319, doi: 10.1111/j.1365-2966.2009.14654.x

Jullo, E., Kneib, J. P., Limousin, M., et al. 2007, New Journal of Physics, 9, 447, doi: 10.1088/1367-2630/9/12/447

Juodžbalis, I., Ji, X., Maiolino, R., et al. 2024, MNRAS, 535, 853, doi: 10.1093/mnras/stae2367

Juodžbalis, I., Marconcini, C., D'Eugenio, F., et al. 2025, arXiv e-prints, arXiv:2508.21748, doi: 10.48550/arXiv.2508.21748

Kaspi, S., Smith, P. S., Netzer, H., et al. 2000, ApJ, 533, 631, doi: 10.1086/308704

Kneib, J. P., Ellis, R. S., Smail, I., Couch, W. J., & Sharples, R. M. 1996, ApJ, 471, 643, doi: 10.1086/177995

Kocevski, D. D., Finkelstein, S. L., Barro, G., et al. 2025, ApJ, 986, 126, doi: 10.3847/1538-4357/adbc7d

Kokorev, V., Caputi, K. I., Greene, J. E., et al. 2024, ApJ, 968, 38, doi: 10.3847/1538-4357/ad4265

Kovačević, J., Popović, L. Č., & Dimitrijević, M. S. 2010, ApJS, 189, 15, doi: 10.1088/0067-0049/189/1/15

Kovačević-Dojčinović, J., Dojčinović, I., Lakićević, M., & Popović, L. Č. 2025, A&A, 694, A289, doi: 10.1051/0004-6361/202450516

Kwan, J., & Krolik, J. H. 1981, ApJ, 250, 478, doi: 10.1086/159395

Labbe, I., Greene, J. E., Matthee, J., et al. 2024, arXiv e-prints, arXiv:2412.04557, doi: 10.48550/arXiv.2412.04557

Landt, H., Bentz, M. C., Ward, M. J., et al. 2008, ApJS, 174, 282, doi: 10.1086/522373

Laor, A., Jannuzi, B. T., Green, R. F., & Boroson, T. A. 1997, ApJ, 489, 656, doi: 10.1086/304816

Lin, X., Fan, X., Cai, Z., et al. 2025, arXiv e-prints, arXiv:2507.10659. https://arxiv.org/abs/2507.10659

Marconi, A., Amiri, A., Feltre, A., et al. 2024, A&A, 689, A78, doi: 10.1051/0004-6361/202449240

Martínez-Aldama, M. L., Panda, S., Czerny, B., et al. 2021, ApJ, 918, 29, doi: 10.3847/1538-4357/ac03b6

Martis, N. S., Sarrouh, G. T. E., Willott, C. J., et al. 2024, https://arxiv.org/abs/2401.01945

Marziani, P., Sulentic, J. W., Plauchu-Frayn, I., & del Olmo, A. 2013, ApJ, 764, 150, doi: 10.1088/0004-637X/764/2/150

Mathews, W. G., & Ferland, G. J. 1987, ApJ, 323, 456, doi: 10.1086/165843

Matsuoka, Y., Kawara, K., & Oyabu, S. 2008, ApJ, 673, 62, doi: 10.1086/524193

Matsuoka, Y., Oyabu, S., Tsuzuki, Y., & Kawara, K. 2007, ApJ, 663, 781, doi: 10.1086/518399

Matsuoka, Y., Oyabu, S., Tsuzuki, Y., Kawara, K., & Yoshii, Y. 2005, PASJ, 57, 563, doi: 10.1093/pasj/57.4.563

Morishita, T., Stiavelli, M., Mason, C. A., et al. 2025, arXiv e-prints, arXiv:2508.01372, doi: 10.48550/arXiv.2508.01372

Naidu, R. P., Oesch, P. A., Brammer, G., et al. 2025, arXiv e-prints, arXiv:2505.11263, doi: 10.48550/arXiv.2505.11263

Netzer, H. 2013, The Physics and Evolution of Active Galactic Nuclei

Netzer, H., & Wills, B. J. 1983, ApJ, 275, 445, doi: 10.1086/161545

Onken, C. A., Ferrarese, L., Merritt, D., et al. 2004, ApJ, 615, 645, doi: 10.1086/424655

Panda, S., Martínez-Aldama, M. L., Marinello, M., et al. 2020, ApJ, 902, 76, doi: 10.3847/1538-4357/abb5b8

Persson, S. E. 1988, ApJ, 330, 751, doi: 10.1086/166509

Planck Collaboration, Aghanim, N., Akrami, Y., et al. 2020, A&A, 641, A6, doi: 10.1051/0004-6361/201833910

Reines, A. E., & Volonteri, M. 2015, ApJ, 813, 82, doi: 10.1088/0004-637X/813/2/82

Richards, G. T., Deo, R. P., Lacy, M., et al. 2009, AJ, 137, 3884, doi: 10.1088/0004-6256/137/4/3884

Rieke, M. J., Robertson, B., Tacchella, S., et al. 2023, 16, doi: 10.3847/1538-4365/acf44d

Rodríguez-Ardila, A., Viegas, S. M., Pastoriza, M. G., Prato, L., & Donzelli, C. J. 2002, ApJ, 572, 94, doi: 10.1086/340192

Rudy, R. J., Mazuk, S., Puetter, R. C., & Hamann, F. 2000, ApJ, 539, 166, doi: 10.1086/309222

Rudy, R. J., Rossano, G. S., & Puetter, R. C. 1989, ApJ, 342, 235, doi: 10.1086/167587

Sacchi, A., & Bogdan, A. 2025, arXiv e-prints, arXiv:2505.09669, doi: 10.48550/arXiv.2505.09669

Sarrouh, G. T. E., Asada, Y., Martis, N. S., et al. 2025, arXiv e-prints, arXiv:2506.21685, doi: 10.48550/arXiv.2506.21685

Shakura, N. I., & Sunyaev, R. A. 1976, MNRAS, 175, 613, doi: 10.1093/mnras/175.3.613

Shen, Y., & Ho, L. C. 2014, Nature, 513, 210, doi: 10.1038/nature13712

Sigut, T. A. A., & Pradhan, A. K. 1998, ApJL, 499, L139, doi: 10.1086/311369

Sigut, T. A. A., & Pradhan, A. K. 2003, ApJS, 145, 15, doi: 10.1086/345498

Smyth, R. T., Ramsbottom, C. A., Keenan, F. P., Ferland, G. J., & Ballance, C. P. 2019, MNRAS, 483, 654, doi: 10.1093/mnras/sty3198

Sulentic, J. W., Zwitter, T., Marziani, P., & Dultzin-Hacyan, D. 2000, ApJL, 536, L5, doi: 10.1086/312717

Taylor, A. J., Kokorev, V., Kocevski, D. D., et al. 2025, arXiv e-prints, arXiv:2505.04609, doi: 10.48550/arXiv.2505.04609

Trefoloni, B., Ji, X., Maiolino, R., et al. 2024, arXiv e-prints, arXiv:2410.21867, doi: 10.48550/arXiv.2410.21867

Tripodi, R., Martis, N., Markov, V., et al. 2024, arXiv e-prints, arXiv:2412.04983, doi: 10.48550/arXiv.2412.04983

Tsuzuki, Y., Kawara, K., Yoshii, Y., et al. 2006, ApJ, 650, 57, doi: 10.1086/506376

Verner, E., Bruhweiler, F., Verner, D., Johansson, S., & Gull, T. 2003, ApJL, 592, L59, doi: 10.1086/377571

Verner, E., Bruhweiler, F., Verner, D., et al. 2004, ApJ, 611, 780, doi: 10.1086/422303

Verner, E. M., Verner, D. A., Korista, K. T., et al. 1999, ApJS, 120, 101, doi: 10.1086/313171

Vestergaard, M., & Peterson, B. M. 2006, ApJ, 641, 689, doi: 10.1086/500572

Vestergaard, M., & Wilkes, B. J. 2001, ApJS, 134, 1, doi: 10.1086/320357

Wills, B. J., Netzer, H., & Wills, D. 1985, ApJ, 288, 94, doi: 10.1086/162767

Yoshii, Y., Tsujimoto, T., & Kawara, K. 1998, ApJL, 507, L113, doi: 10.1086/311690

Yue, M., Eilers, A.-C., Ananna, T. T., et al. 2024, ApJL, 974, L26, doi: 10.3847/2041-8213/ad7eba